Numerical Simulation of Bubble Dynamics in a Vortex Flow Using Navier-Stokes Computations and Moving Chimera Grid Scheme

Chao-Tsung Hsiao and Georges L. Chahine
DYNAFLOW, INC.
10621-J Iron Bridge Road, Jessup, MD 20794
email: info@dynaflow-inc.com **http://www.dynaflow-inc.com**

Abstract

A numerical scheme using Navier-Stokes computations was applied to simulate bubble dynamics in a vortex flow. A moving grid generation scheme and a Chimera grid scheme were integrated with the Navier-Stokes solver to automatically generate the appropriate grids based on the moving bubble surface. A general free surface boundary condition was implemented to describe the bubble surface motion. The numerical scheme was validated by comparing results with those obtained from the Rayleigh-Plesset equation and from the potential flow solver, *3DynaFS*, for bubble dynamics in an infinite volume of quiescent water with/without the gravity effect. Important numerical factors that influenced the accuracy of solution are reported. Finally, the computations were conducted for bubbles released within a Rankine vortex. Different bubble behaviors were observed for different cavitation numbers.

1. Introduction

Tip vortex cavitation is of critical importance due to its impact on the noise production of a propeller. In order to avoid or control cavitation, researchers are required to understand what mechanisms lead to cavitation inception of the tip vortex. From previous experimental observations (Arndt and Maines 2000), the cavitation inception appears to start with a quasi-spherical nucleus, which is drawn into the vortex core from the free stream and grows significantly. As the bubble approaches the vortex core, non-spherical deformations become significant. The bubble may then become multi-connected during its capture and break up into multiple bubbles Chahine (1990, 1995). Near the vortex centerline the bubble elongates in the axial direction and may get broken into segments as it travels downstream and becomes centered on the vortex axis. From detailed experimental observations, Gopalan et al. (2000) even suggested that the distorted-bubble break-up emits much higher amplitude noise than mere changes to bubble size and shape.

To numerically predict the cavitation inception accurately, one must take into account the non-spherical deformation and the bubble/vortex interaction. However, most previous studies on numerical simulations of bubble capture by a tip vortex were primarily limited to the spherical bubble model which assumes that the bubble does not interact with the underlying flow field and remains spherical during capture. Ligneul and Latorre (1989) applied this approach to deduce noise emission from cavitation in a Rankine line vortex. Hsiao and Pauley (1999) further applied this approach to study tip vortex cavitation inception with the tip vortex flow field computed by a Reynolds-Averaged Navier-Stokes solver. This has the disadvantage of neglecting bubble/flow interaction and any acoustical signal due to non-spherical deformations. A non-spherical bubble dynamics model based on the boundary element method was first developed by Chahine (1990, 1995) to study the non-spherical deformation of the bubble during capture by a line vortex by neglecting the effect the bubble has on the underlying vortex flow field. Later, a modified dual reciprocity boundary element method was developed and the vortical flow field was simulated by a Vortex Element Method (Chahine *et al*, 1997). Although this method can simulate the bubble/vortex interaction, the underlying vortex flow field must be provided beforehand and is not part of solution. To account in a more direct way for the full viscous interaction between the bubble and the vortex, a direct numerical simulation of bubble dynamics in a vortex flow using Navier-Stokes computations is required.

The goal of the current study is to advance the understanding of bubble dynamics in a complex real fluid flows. To achieve this goal, we develop a three-dimensional incompressible Navier-Stokes flow solver (DFI-UNCLE), which is based on the flow solver UNCLE developed at the Mississippi State University (Arabshahi *et al*. 1995). In DFI-UNCLE, a general free surface boundary condition is implemented to describe the bubble surface. Since the bubble surface is a moving boundary, a moving grid generation scheme which can automatically generates an appropriate grid based on new boundaries is integrated with the Navier-Stokes solver. Our ultimate objective is to simulate the bubble dynamics in a vortex flow generated by a marine propulsor. However, it is difficult to automatically construct a global structured grid that has a mesh smoothly patched to both the propulsor boundaries and the bubble surface even with a multi-block structured grid scheme. To overcome this problem, we implement a Chimera grid scheme, a composite grid scheme, in which an overset grid is created independently of the global grid to encompass the moving bubble without requiring mesh boundaries to join in any special way. The Navier-Stokes computations are then conducted separately for each grid domain and the information between the two domains is exchanged by interpolation at the grid boundaries.

2. Computational Method

2.1 Computational Domain and Grid Generation

In order to well describe the bubble dynamics, an O-type surface grid is generated on the bubble. An O-O type 3D domain grid is generated to extend the grid from the bubble surface to the far-field boundary which we arbitrarily locate at 800 R_0 (R_0 is the initial bubble radius) when a single block grid is used. When a Chimera composite grid is used, the outer boundary of the bubble grid is located at 25 R_0. Such a 3D O-O type grid is shown in Figure 1.

Since the bubble moves and its surface deforms during the numerical simulation, an efficient grid generation scheme that can automatically generate an appropriate grid based on the moving boundary at each time step must be integrated with the Navier-Stokes Solver. A grid generation scheme combining both algebraic and elliptic grid generation techniques as described by Hsiao (1996) is applied. This grid generation scheme is selected because the algebraic grid generation technique is suited to create a clustering and boundary-orthogonal grid at the bubble surface which is important for resolving the flow field near the bubble surface and for applying appropriate free surface boundary conditions. The Elliptic grid generation technique is then applied to smooth out the rough algebraic grid.

With the current grid generation, the first grid spacing from the bubble surface is kept as a constant (=0.001 R_0) during computation. To avoid uneven distribution of the surface grid points due to bubble deformation, a re-gridding scheme is applied every few time steps at the bubble surface to restore the grid distribution according to the initial grid-stretching factor.

2.2 Navier-Stokes Computations

The unsteady incompressible continuity and Navier-Stokes equations written in non-dimensional form and Cartesian tensor notations are given as

$$\frac{\partial u_i}{\partial x_i} = 0 \,, \tag{1}$$

$$\frac{\partial u_i}{\partial t} + u_j \frac{\partial u_i}{\partial x_j} = -\frac{\partial \hat{p}}{\partial x_i} + \frac{1}{\mathrm{Re}} \frac{\partial^2 u_i}{\partial x_j \partial x_j} \,, \tag{2}$$

where $u_i = (u, v, w)$ are the Cartesian components of the velocity, $x_i = (x, y, z)$ are the Cartesian coordinates, $\hat{p} = p + z/\mathrm{Fr}^2$ is the reduced dynamic pressure, p is the pressure, $\mathrm{Fr} = u^*/\sqrt{gL^*}$ is the Froude number, $\mathrm{Re} = \rho u^* L^*/\mu$ is the Reynolds number, u^* and L^* are the characteristic velocity and length, g is the acceleration of gravity, ρ is the liquid density, and μ is its dynamic viscosity. If the gravity effects are neglected, then the reduced dynamics pressure is equal to the pressure. Since a boundary-fitted curvilinear grid is generated in order to simulate a flow with a moving free surface, Equations (1) and (2) must be transformed into a general curvilinear coordinate system. The transformation will provide a computational domain that is better for applying the spatial differencing scheme and the boundary conditions.

To solve the transformed equations, the three-dimensional incompressible Navier-Stokes flow solver, UNCLE, developed at Mississippi State University is modified and used. The UNCLE code is based on the artificial-compressibility method (Chorin 1967) in which a time derivative of pressure is added to the continuity equation as

$$\frac{1}{\beta} \frac{\partial \hat{p}}{\partial t} + \frac{\partial u_i}{\partial x_i} = 0 \,, \tag{3}$$

where β is the artificial compressibility factor. As a consequence, the hyperbolic system of Equations (2) and (3) is formed and can be solved using a time marching scheme. This method can be marched in pseudo-time to reach a steady-state solution. To obtain a time-dependent solution, a Newton iterative procedure needs to be performed in each physical time step in order to satisfy the continuity equation. The numerical scheme in UNCLE uses a finite volume formulation. The first-order Euler implicit difference formula is applied to the time derivatives. The spatial differencing of the convective terms uses the flux-difference splitting scheme based on Roe's method (Roe, 1981) and van Leer's MUSCL method (van Leer, 1979) for obtaining the first-order and the third-order fluxes respectively. A second-order central differencing is used for the viscous terms, which are simplified using a thin-layer approximation. The flux Jacobians required in an implicit scheme are obtained numerically. The resulting system of algebraic equations is solved using the Discretized Newton Relaxation method (Vanden and Whitfield, 1993) in which symmetric block Gauss-Seidel sub-iterations are performed before the solution is updated at each Newton interaction.

2.3 Chimera Grid Scheme

The Chimera grid scheme is a grid embedding technique, which provides a conceptually simple method for domain decomposition. In this approach, structured subgrids generated around each component in the flow field or over subdomains of complex geometries are put together without requiring the mesh boundaries to join in any special way. In the present study, a body-fitted subgrid is created around the bubble while a global rectangular grid is created for the global flow field. Figure 2 illustrates the Chimera grid system in a two-dimensional domain. In the Chimera grid system, the global grid consists of three different types of points; regular, overlap and hole points, and the subgrid consists of two different types of points; regular and overlap points. The Navier-Stokes equations are solved separately for global grid and subgrid at all regular points. The communication between these two grids is made by interpolating flow variables at the overlap points.

Data from the global grid are interpolated to supply outer boundary conditions to the subgrid. Hence the effect of the main flow field is properly imposed on the bubble. For the global grid solution to account for the bubble, points in the global grid are blanked out to form the hole within some neighborhood of the bubble. On the fringes of this blanked-out region, data from the subgrid solution are interpolated to serve as interior boundary conditions for the global grid. Thus, the presence of the bubble is imposed on the main flow field.

The implementation of the Chimera grid scheme includes two tasks: 1) identify the hole and the overlap points, 2) determine the interpolation stencil and interpolation coefficients. The hole is typically defined by a creation boundary which consists of the grid surface at constant z in the current study. A global grid point is considered to be a hole point if it is inside the creation boundary. A grid point is considered to be inside the creation boundary if the dot product between the vector from the closest point at the boundary to the grid point and the normal vector at the boundary at the closest point is negative or zero. The overlap points of global grid are then determined based on the hole fringe. Here, two layers of grid stencil are identified as the overlap points to implement the third order boundary condition.

To determine the interpolation stencil from the background grid for each overlap point, a three-dimensional point-locating scheme is implemented. The locating scheme is based on the fact that the coordinates (x, y, z) of each overlap point may uniquely be represented by 8 corner points of a grid stencil from background grid

$$x=\sum_{i=1}^{8} N_i \overline{x}_i, \quad y=\sum_{i=1}^{8} N_i \overline{y}_i, \quad z=\sum_{i=1}^{8} N_i \overline{z}_i \quad \text{where} \quad \begin{cases} N_1=(1-f)(1-y)(1-j), & N_2=f(1-y)(1-j), \\ N_3=(1-f)y(1-j), & N_4=fy(1-j), \\ N_5=(1-f)(1-y)j, & N_6=f(1-y)j, \\ N_7=(1-f)yj, & N_8=fyj, \end{cases} \tag{4}$$

and f, y, j are the interpolation coefficients, and $(\overline{x}_i, \overline{y}_i, \overline{z}_i)$ are the coordinates of eight corner points of a grid stencil in the background grid. Equation (4) is solved using Newton-Raphson method. For the overlap point to be inside the grid stencil, it will require $0 \le x \le 1, 0 \le h \le 1, 0 \le z \le 1$. The search process for each overlap point is described below:

Step 1. Find the closest point from the background grid as an initially guessed pivot point.
Step 2. Apply the Newton-Raphson Method to obtain f, y, j .
Step 3. Check if f, y, j are between 0 and 1: Yes: mark the pivot point, save f, y, j , and go to Step 6. No: go to Step 4.
Step 4. Chose another pivot point by jumping to the neighboring point based on the values of f, y, j .
Step 5. Go to Step 2.
Step 6. Use the current pivot point as the initial guess of next search and go to step 2.

In addition to the two tasks described above, a blanking technique is implemented in the Navier-Stokes solver to account for holes and interior boundaries and to account for boundary data transfer from the interpolation data set rather than from the usual boundary conditions. In the iterative solution routines, a variable

$$ib(i,j,k)=\begin{cases} 1, & \text{if a point is not blanked} \\ 0, & \text{if a point is blanked} \end{cases}, \tag{5}$$

is introduced to blank out the hole and overlap points such that no update of the variables takes place at these points. In the original UNCLE code, the system of linear equations is written to solve for the flow variable difference, ΔQ, between iterations and to update the flow variables by $Q^{n+1}=Q^n+\Delta Q$. To ensure that ΔQ equals to zero at blanked points, we multiply the matrix coefficients of the left hand side and the vector of right hand by ib and assign the diagonal terms of the matrix to be one for $ib=0$.

2.4 Boundary Conditions

There are two types of boundaries where conditions have to be specified in the present study. One concerns the physical boundaries of the problem considered and the other concerns the boundaries of the grid topology used for mapping the physical space to the computational space. In addition, if an overset grid scheme is applied, an interpolation boundary condition needs to be applied at the overlap points.

2.4.1 *Physical Boundary Conditions*

The physical boundary conditions include a free stream boundary condition required to specify the boundary far away from the bubble surface and a free surface boundary condition required to specify the bubble surface boundary. The free stream boundary condition is applied by assuming that the computational domain is large enough such that the perturbation in the flow field due to the bubble is negligible at the far field boundary.

To best describe the bubble surface behavior, a general free surface boundary condition satisfying both kinematic and dynamic boundary conditions is implemented. The kinematic boundary is the Lagrangian condition that a particle on the surface must remain on the surface. Instead of using the Lagrangian condition directly to update the bubble surface by moving surface grid points based upon their velocities, a curvilinear Eulerian kinematic boundary condition is applied. To directly obtain a curvilinear Eulerian kinematic boundary condition, we define F as a scalar function for the free surface in curvilinear coordinates such that

$$F(x_i,t)=z-H(x,h,t)=0, \tag{6}$$

where $x_i = (x, h, z)$ are the non-inertial curvilinear coordinates at time *t* and *H* is the distance to the bubble surface measured from $z = 0$ along a line of constant x and h. This implies that the bubble surface is defined by the $z = 0$ surface and the variation of the bubble surface can be determined by the distance *H*. To satisfy the kinematic boundary condition we have

$$\frac{DF}{Dt} = \frac{\partial F}{\partial t} + U_i \frac{\partial F}{\partial x_i} = 0 , \tag{7}$$

where $U_i = (U, V, W)$ are the contravariant velocity components obtained by

$$U_i = u_i x_i + \frac{\partial x_i}{\partial t} . \tag{8}$$

Substituting Equation (6) in to Equation (7) provides the general curvilinear Eulerian kinematic boundary condition in curvilinear coordinates as

$$\frac{\partial H}{\partial t} = \left(W - \frac{\partial z}{\partial t} \right) - U \frac{\partial H}{\partial x} - V \frac{\partial H}{\partial h} . \tag{9}$$

Equation (9) can be solved implicitly for H^{n+1} at the new time step. This implies that the grid points on the bubble surface will move along z direction with $H^{n+1} - H^n$ in the computational space. To update the grid points on the bubble surface in the physical space at the new time step, we use

$$x_i^{n+1} = x_i^n + \left(H^{n+1} - H^n \right) \frac{\partial x_i}{\partial z} . \tag{10}$$

The general free surface dynamic boundary condition is the condition of zero shear stress and normal stress balance at the bubble surface when the stress due to the gas inside the bubble is neglected. With the same simplifications used by Batchelor (1967) for deriving the dynamic boundary condition in the Cartesian coordinate system, Hodges *et al*. (1996) derived a dynamic boundary condition in a curvilinear coordinate system by requiring the grid to be normal to the boundary. Following their work the current study implements the dynamic boundary condition as

$$\frac{\partial U}{\partial z} = -g_{33} \left(g^{11} \frac{\partial W}{\partial x} + g^{12} \frac{\partial W}{\partial h} \right), \tag{11}$$

$$\frac{\partial V}{\partial z} = -g_{33} \left(g^{22} \frac{\partial W}{\partial h} + g^{12} \frac{\partial W}{\partial x} \right), \tag{12}$$

$$\hat{p} = p_g + p_v + \frac{z}{\mathrm{Fr}^2} - \frac{1}{\mathrm{Re}} \frac{\partial W}{\partial z} - \frac{C}{\mathrm{We}} , \tag{13}$$

with

$$g^{ij} = \frac{\partial x_i}{\partial x_k} \frac{\partial x_j}{\partial x_k}, \qquad g_{ij} = \frac{\partial x_i}{\partial x_k} \frac{\partial x_j}{\partial x_k} , \tag{14}$$

where *C* is the curvature, $\mathrm{We} = r u^{*2} L^* / g$ is the Weber number, g is the surface tension, and p_v is the vapor pressure, and p_g is the gas pressure. To determine the gas pressure we assume that the amount of non-condensible gas inside the bubble remains constant and the gas satisfies the polytropic relation $p_g u^k = \text{constant}$, where u is the bubble volume and *k* is the polytropic constant. For illustration purposes, *k* = 1 for isothermal behavior is used in the present study.

2.3.3 ***Grid Topology Boundary Conditions***

Since the O-O type grid is used in the present study, two additional boundary conditions due to grid topology needs to be imposed (see Figure 1). In the O-O type grid two singular axes along which grid points collapse into one single point in the physical space are mapped into two boundaries (*i.e.* $x = 0$ and $x = 1$) in the computational space. Since we are using a finite volume scheme, the Dirichlet type boundary condition is imposed by specifying the value of the variables at imaginary points outside the boundary as

$$Q_0 = 2Q_b - Q_1 , \tag{13}$$

where Q_0 is the value at an imaginary point, Q_b is at the boundary, and Q_2 is at the first interior cell center from the boundary. To treat the singular axis boundary, Q_b is computed by

$$Q_b = \frac{1}{(N-1)} \sum_{j=1}^{N-1} \left(1.5 Q_{1,j} - 0.5 Q_{2,j} \right) , \tag{14}$$

where Q_2 is the value at the second interior cell center from the boundary and N is the number of grid points in the h direction.

The other boundary due to the grid topology is the cut interface on which grid points from two boundaries (*i.e.* $h = 0$ and $h = 1$) in the computational space share the same location in the physical space. To treat the cut interface

boundary, the value of the imaginary point on each boundary is assigned naturally to be the value of the first interior cell center from the other boundary.

For the boundary condition at the overlap points, the flow variables are computed by

$$Q = \sum_{i=1}^{8} N_i \bar{Q}_i \ , \tag{15}$$

where N_i is defined in Equation (4), and $\bar{Q}_i$ are the values of flow variables at eight corner points of corresponding grid stencil in the background grid.

3. Results

3.1 Validation

Before applying the current numerical method to simulate a bubble moving inside a vortex flow, we simulate bubble dynamics in an infinite volume of quiescent water and compare the results to the solution obtained with the Rayleigh-Plesset equation (Plesset, 1948). In this case we consider a bubble with an initial radius, R_0, equal to 0.01m and an initial gas pressure equal to 5 times the ambient pressure, p_{amb}, which is equal to one atmosphere pressure. The characteristic length and velocity are selected to be R_0 and $\sqrt{p_{amb}/r}$ respectively. The gravity is neglected such that the bubble grows and collapses spherically. For the computations conducted in this section, we use an O-O type single block grid which is composed of a total of 35301 points in which 41×21 grid points are generated on the bubble surface and 41 grid points are generated in the radial direction.

Our computations show that the solution of the Navier-Stokes equations highly depends on the initial conditions selected and on the artificial compressibility factor as shown in Figure 3. It is noted that all results are shown in non-dimensional form in the following figures. The Navier-Stokes computation were first conducted with an initial condition of quiescent water in which the velocity was everywhere equal to zero and the pressure was equal to the ambient pressure. The results show that the Navier-Stokes computations significantly under-predict the variation of the bubble radius. To improve the solution an initial condition satisfying the Rayleigh-Plesset equation at the first time step is applied, that is the correct relationship between R_0, the bubble wall velocity, and p_{g0} is used. Figure 3a shows the comparison of the bubble radius versus time between the Rayleigh-plesset and the Navier-Stokes computations for different initial conditions and for $b = 100$. In addition, our computations also show that the artificial compressibility factor is also very important for the simulations. In Figure 3a, the solution of the Navier-Stokes computation was obtained with $b = 100$. By increasing b to 1000, it is found that the solution of the Navier-Stokes computation agrees much better with the Rayleigh-Plesset exact solution as seen in Figure3b.

To further validate the current numerical scheme, gravity is taken into account in the next simulations. From previous bubble explosion studies, it is know that with the gravity effect the bubble moves upward due to the buoyancy force, and a reentrant jet is formed during the bubble collapse. In this case we consider a bubble with an initial radius equal to 0.01m and an initial gas pressure equal to 81.6 times the ambient pressure and a Froude number, F= 32.14. To validate the result, the solution of the Navier-Stokes computation is compared to the solution of *3DynaFS*. *3DynaFS* is a three-dimensional potential flow solver which is based on the Boundary Element Method (Chahine et al., 1989). For both methods the simulations are terminated when the reentrant jet touches the opposite bubble surface. Figure 4a shows the comparison of the bubble volume versus time between the *3DynaFS* and the DFI-UNCLE computations. The locus of both bubble top and bottom points versus time for both computations are also shown in Figure 4b. It is seen that the comparison shows a good agreement. The pressure field and velocity vectors are shown in Figure 5 when the reentrant jet touches the opposite bubble surface. It is seen that the reentrant jet carries a flow with high pressure and velocity at the time it touches the opposite bubble surface.

3.2 Bubble Dynamics in a Vortex Flow

This section shows results of numerical simulations of bubble dynamics in a vortex flow for a bubble released in an initially prescribed Rankine line vortex with and without axial velocity. The Rankine vortex has a core of size, a_c = 0.00508m, and circulation strength, $\Gamma = 0.4426\text{m}^2/\text{s}$. The characteristic length and velocity are equal to a_c and $\Gamma/2\pi a_c$. This results in a pressure coefficient $Cp_{\min} = -2$ at the vortex center. The computations were first conducted for a bubble of R_0 = 200μm released at the vortex center with cavitation number, $s = 2.0$ and without axial velocity. Gravity is neglected in this simulation. The initial internal pressure inside the bubble is taken to be equal to the pressure at infinity, which is much larger than the pressure on the vortex axis, and the bubble is left free to adapt to this pressure difference. Figure 6 shows the bubble shapes at various times for different cavitation numbers. It is apparent that during the initial phase of the bubble growth, the bubble grows almost spherically. Later on, the bubble shape starts to depart from spherical and to adapt to the pressure field. Once the bubble has exceeded its equilibrium volume, the bubble surface is forced back towards its initial position. Figure 7 shows the bubble volume oscillations. Since the bubble surface portions away from the axis and near the axis encounter different pressure filed, they returns to the initial positions in different phases. To illustrate the bubble oscillations in non-spherical shapes, the locus of four bubble pole points are plotted in Figure 8 for $s = 2.0$.

To generalize the numerical simulation of bubble dynamics in a vortex flow, we release a bubble away from the vortex center in a Rankine line vortex with axial velocity. Instead of using an O-O type single block grid, we use Chimera composite grids which include a rectangular global grid of $61\times31\times31$ points for the flow field and an O-O type grid of $41\times21\times25$ for the moving bubble. The computations are conducted for a bubble of $R_0 = 200\mu m$ released at $0.2a_c$ away from the vortex center with the initial bubble surface velocity equal to the local velocity and the initial internal bubble pressure equal to the pressure at infinity. The axial velocity is set to $\Gamma/2\pi a_c$ and the cavitation number is equal to $-Cp_{\min}$ in this case. The simulation shows that while the bubble rotates around the vortex center, it elongates and a reentrant jet forms with a direction toward the vortex center. Figure 9 shows the bubble shapes and locations during capture by vortex. The pressure and velocity vectors at different times are shown in Figure 10. It is seen that the vortex flow filed around the bubble is altered by the bubble. It is noted that the result in Figure 10 was plotted only in the subgrid at constant h plane, *i.e.* at the bubble middle section. It is seen that during computation the size and location of the subgrid were adjusted according to the bubble size and location.

4. Conclusions

We have developed a numerical code, DFI-UNCLE, derived from the Mississippi State University Navier-Stokes Solver UNCLE to simulate bubble dynamics in a vortex flow. The numerical schemes implemented in the DFI-UNCLE were validated by comparing the results with those obtained from Rayleigh-Plesset equation and from *3DynaFS*. Our computations show that the solution of the Navier-Stokes computations for bubble dynamics in an infinite volume of quiescent water highly depends on the initial condition and on the artificial compressibility factor. With an appropriate initial condition and a compressibility factor, the comparison showed a very good agreement.

The simulation of bubble dynamics in a vortex flow was conducted by releasing a bubble inside a Rankine line vortex. The non-spherical bubble deformation due to the bubble/vortex interaction was demonstrated for a bubble released at the vortex center. To demonstrate the feasibility of DFI-UNCLE, we simulated the bubble capture by a line vortex by releasing a bubble away the vortex center in a Rankine line vortex with axial velocity. The simulations showed that the bubble elongates and a reentrant jet forms with a direction toward the vortex center when it travels downstream and towards the vortex center. These results are similar to those obtained with *3DynaFS*. Future detailed comparisons between the two codes will be made to extract the importance of the viscous interaction.

Acknowledgements

This work was conducted at DYNAFLOW, INC. and has been supported by Office of Naval Research under the contract No. N0014-99-C-0369 monitored by Dr. Edwin P. Rood. This support is greatly appreciated. We also are grateful for the Mississippi State University, Prof. Whitfield for providing us with the code UNCLE under the above-quoted ONR contract.

References

Arabshahi, A., Taylor, L.K., Whitfield, D.L., "UNCLE: Toward a Comprehensive Time Accurate Incompressible Navier-Stokes Flow Solver, AIAA-95-0050, 1995.

Arndt, R.E and Maines, "Nucleation and Bubble Dynamics in Vortex Flows," *ASME Journal of Fluids Engineering*, Vol. 122, pp. 488-493, 2000.

Batchelor, G.K., *Fluid Dynamics*, Cambridge University Press, 1967.

Chahine, G.L., "Nonspherical Bubble Dynamics in a Line Vortex," The ASME Cavitation and Multiphase Flow Forum, Toronto, Canada, Vol. 98, pp. 121-126, June 1990.

Chahine, G.L., Perdue, T.O., Tucker, C.B., "Interaction Between Underwater Explosion Bubble and a Solid Submerged Body," DYNAFLOW, INC. Technical Report 89001-1, August, 1989.

Chahine, G. L., "Bubble Interaction with Vortices," Vortex Flow, Chapter 18, Ed. S. Green, Kluwer Academic, 1995.

Chahine, G.L., Sarkar, K., and Duraiswami, R., "Strong Bubble/Flow Interactions and Cavitation Inception," DYNAFLOW, INC. Technical Report 94003-1ONR March 1997.

Chorin, A.J., "A Numerical Method for Solving Incompressible Viscous Flow Problems," *Journal of Computational Physics*, Vol. 2, pp. 12-26, 1967.

Gopalan, S., Liu, H.L., and Katz, J., "On the Flow Structure, Tip Leakage Cavitation Inception and Associated Noise," 23rd Symposium on Naval Hydrodynamics, Sep. 17-22, France, 2000.

Hodges, B. Street, R. Zang, Y., "A Method for Simulation of Viscous, Nonlinear, Free-Surface Flows," 20th *Symposium on Naval Hydrodynamics*, pp. 791-809, 1996.

Hsiao, C.-T., Pauley, L.L., , "Study of Tip Vortex Cavitation Inception Using Navier-Stokes Computation and Bubble Dynamics model," *ASME Journal of Fluid Engineering*, Vol. 121, pp. 198-204, 1999.

Hsiao, C.-T., "Numerical Study of the Tip Vortex Flow Over a Finite-Span Hydrofoil, " Ph.D. Thesis, Department of Mechanical Engineering, The Pennsylvania State University, Adviser L.L. Pauley, 1996.

Ligneul, P., Latorre, R., "Study on the Capture and Noise of Spherical Nuclei in the Presence of the Tip Vortex of Hydrofoils and Propellers," *Acustica*, Vol. 68, pp.1 14, 1989.

Plesset M.S., "Dynamics of Cavitation Bubbles," *Journal of Applied Mechanics*, Vol. 16, pp.228-231.
Roe, O.L., "Approximate Riemann Solvers, Parameter Vectors and Difference Schemes," *Journal of Computational Physics*, Vol. 43, pp. 357-372, 1981.
Vanden, K., Whitfield, D.L., "Direct and Iterative Algorithms for the Three-Dimensional Euler Equations," AIAA-93-3378, 1993.
Van Ieer, B., "Towards the Ultimate Conservative Difference Scheme. V. A Second Order Sequel to Godunov's Method," *Journal of Computational Physics*, Vol. 32, pp. 101-136, 1979.

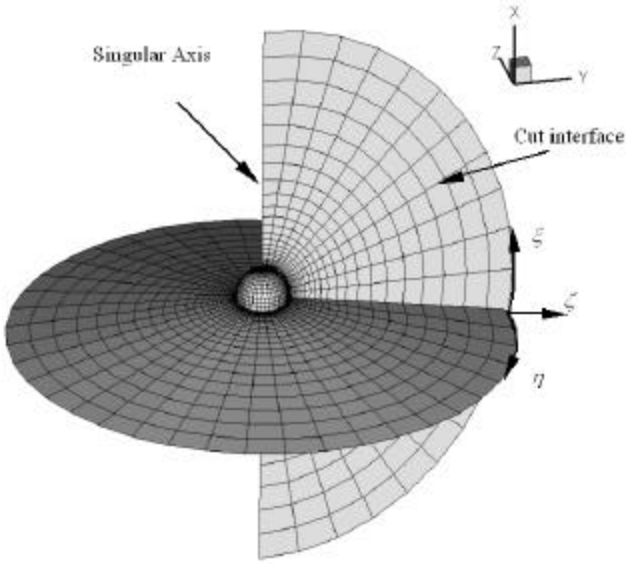

Figure 1. 3D O-O type grid used to describe the domain around the dynamics bubble.

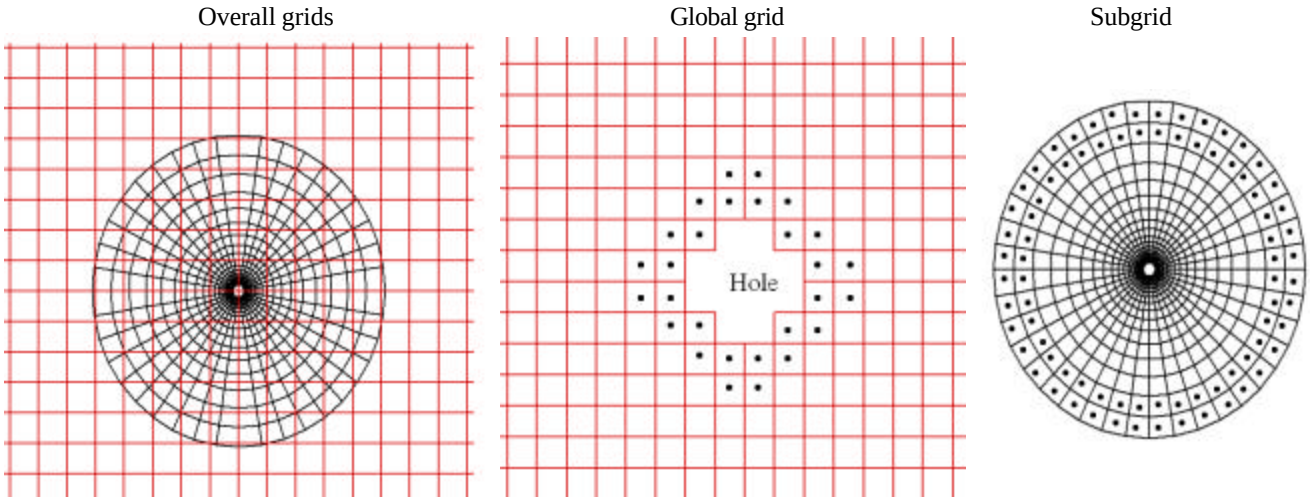

Figure 2. Illustration in 2D of the Chimera grid system and localization of the hole and of overlap points marked as • .

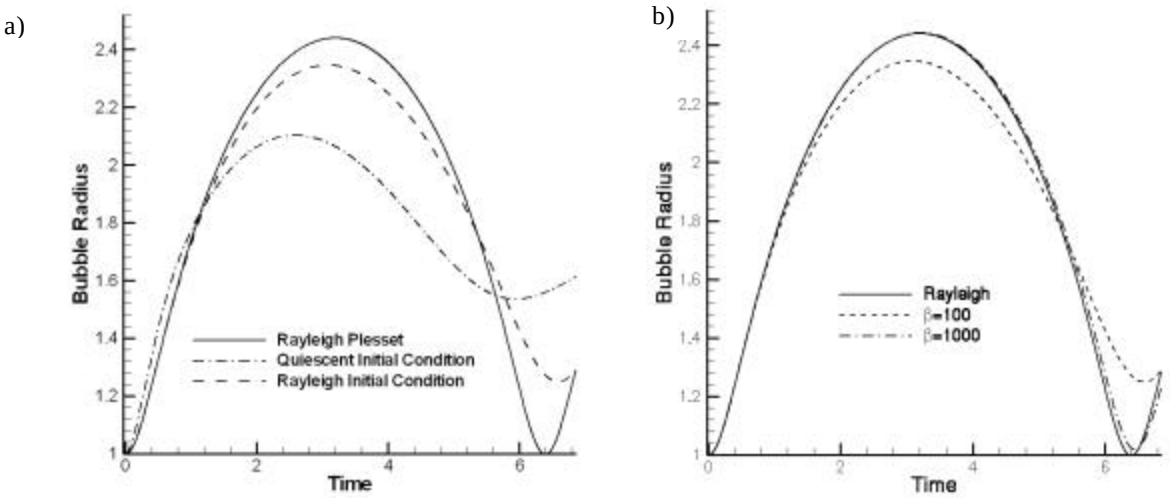

Figure 3. Comparison of bubble radius history obtained by DFI-UNCLE for a) various initial conditions b) various compressibility factors b for R_0=0.01m, p_{g0}/p_∞=5.

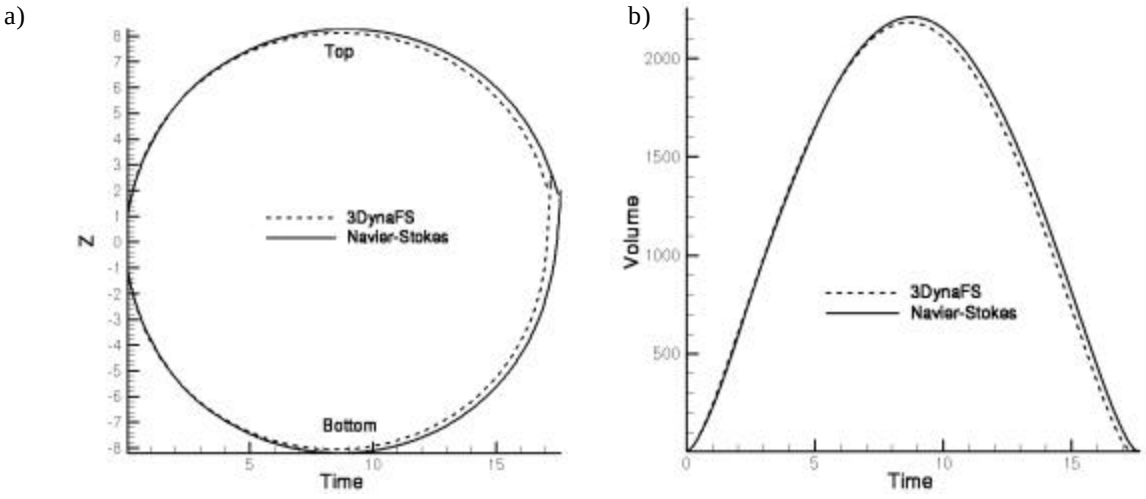

Figure 4. Comparison between *3DynaFS* and DFI-UNCLE computations for a) bubble pole motion b) bubble volume history for a bubble in gravity field, R_0=0.01m, p_{g0}/p_∞=81.6 and F=32.14.

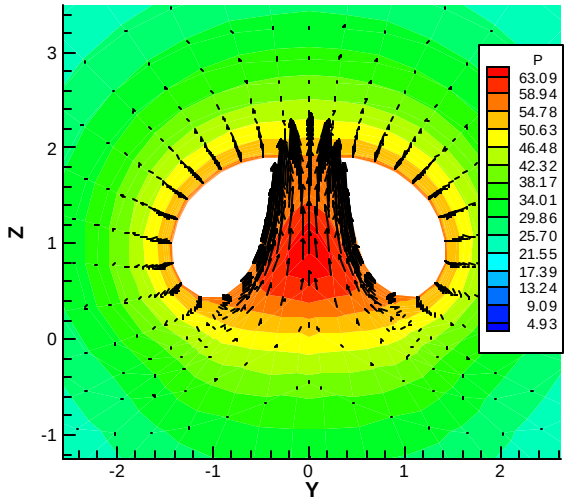

Figure 5. Pressure contour and velocity vector obtained with DFI-UNCLE when the reentrant jet touch the bubble surface for the same case as in Figure 4, R_0=0.01m, p_{g0}/p_∞=81.6 and F=32.14.

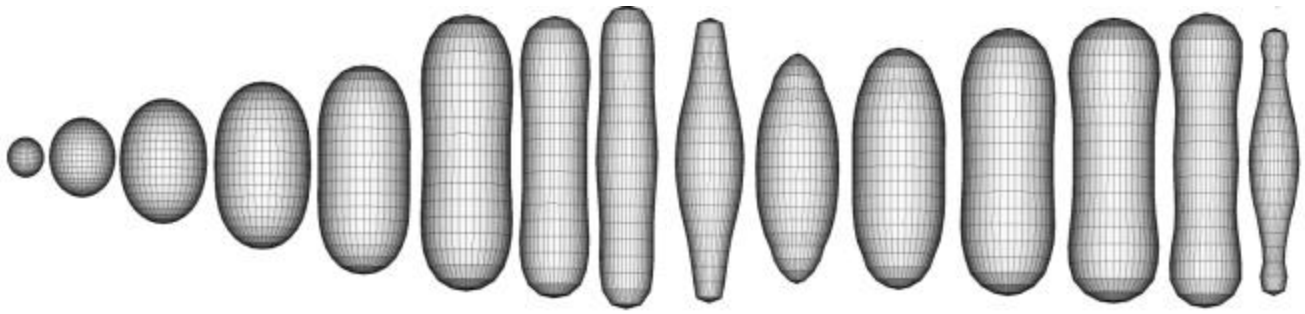

Figure 6. Shape history for bubble on vortex axis obtained with DFI-UNCLE for R_0=200μm, p_{g0}/p_∞=1 and $s = 2.0$.

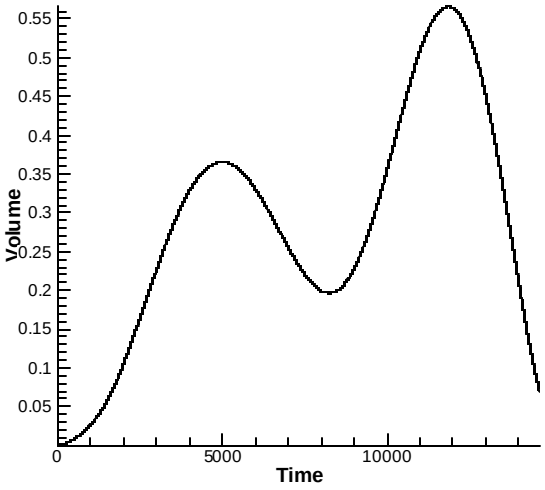

Figure 7. Bubble on vortex axis volume history obtained with DFI-UNCLE for R_0=200μm, p_{g0}/p_∞=1 and $s = 2.0$.

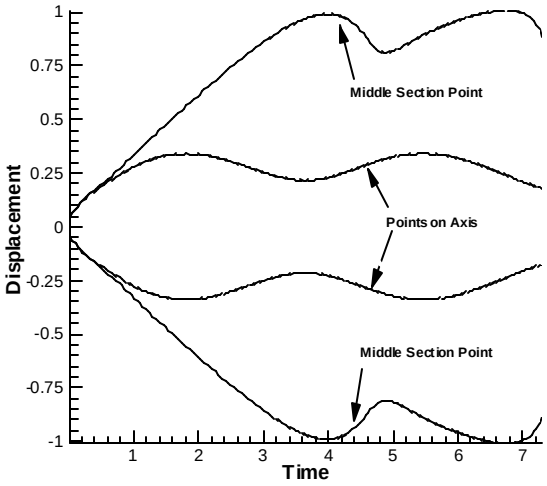

Figure 8. The locus of four bubble pole points obtained with DFI-UNCLE for the same case as in Figures 6 and 7, R_0=200μm, p_{g0}/p_∞=1 and $s = 2.0$.

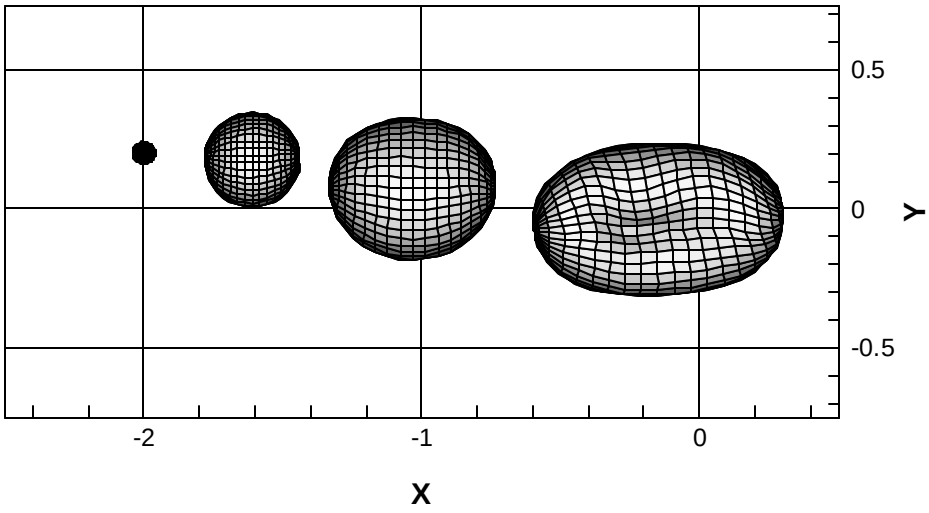

Figure 9. Bubble shape and location during its capture by a line vortex as obtained with DFI-UNCLE for bubble initially off the vortex center, R_0=200μm, p_{g0}/p_∞=1 and $s = 2.0$.

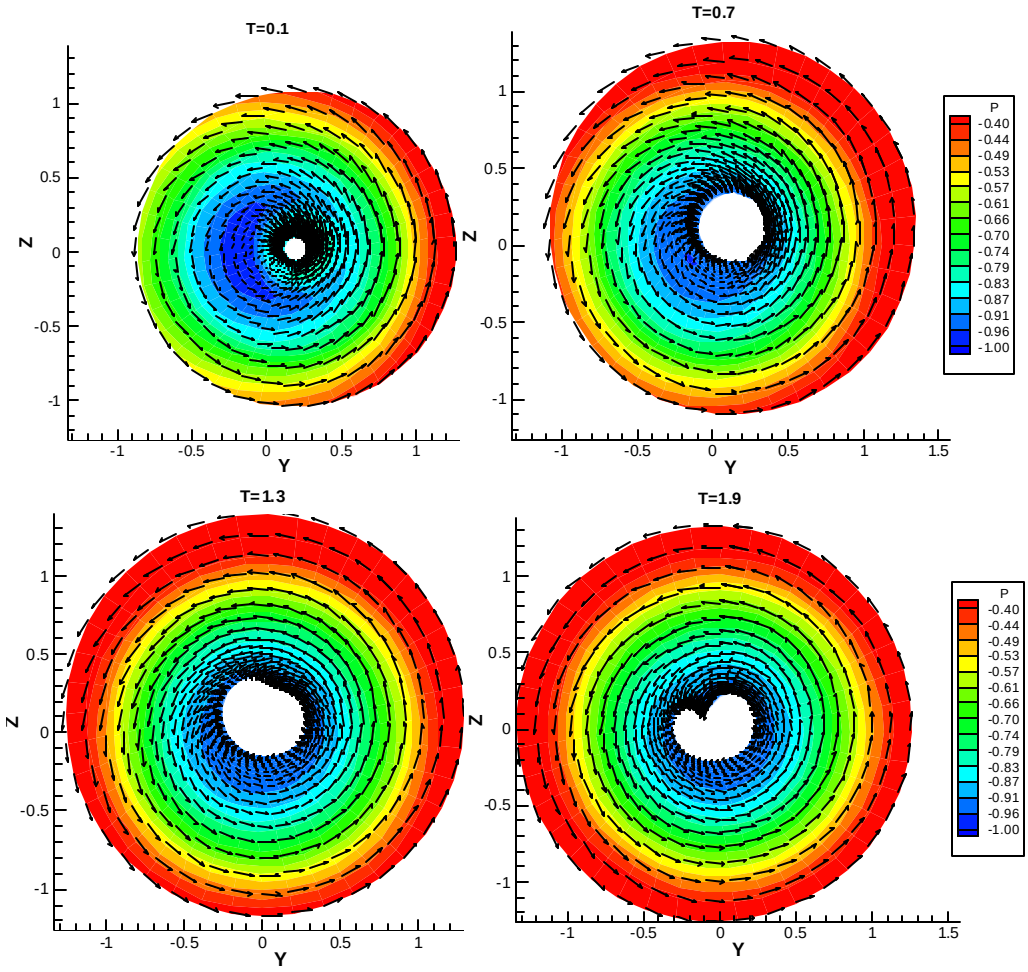

Figure 10. Pressure contour and velocity vector obtained at different times for the same bubble as in Figure 9, R_0=200μm, p_{g0}/p_∞=1 and $s = 2.0$.